Optical properties of metallic MXene multilayers through advanced first-principles calculations

Zafer Kandemir,[1] Pino D'Amico,[2] Giacomo Sesti,[2] Claudia Cardoso,[2,*] Milorad V. Milošević,[3,4] and Cem Sevik[3,†]

[1]*Faculty of Engineering and Natural Sciences, Sabanci University, 34956 Istanbul, Turkey*

[2]*CNR-NANO Research Center S3, Via Campi 213/a, 41125 Modena, Italy*

[3]*Department of Physics and NANOlight Center of Excellence, University of Antwerp, Groenenborgerlaan 171, B-2020 Antwerp, Belgium*

[4]*Instituto de Física, Universidade Federal de Mato Grosso, Cuiabá, Mato Grosso 78060-900, Brazil*

(Received 29 April 2024; accepted 2 July 2024; published 22 July 2024)

Having a strong electromagnetic absorption, MXene multilayers are readily envisaged for applications in electromagnetic shields and related prospective technology. However, an *ab initio* characterization of the optical properties of MXenes is still lacking, due in part to major difficulties with the treatment of metallicity in the first-principles approaches. Here we addressed the latter challenge, after a careful treatment of intraband transitions, to present a thorough analysis of the electronic and optical properties of a selected set of metallic MXene layers based on density functional theory (DFT) and many-body perturbation theory calculations. Our results reveal that the *GW* corrections are particularly important in regions of the band structure where *d* and *p* states hybridize. For some systems, we show that *GW* corrections open a gap between occupied states, resulting in a band structure that closely resembles that of an intrinsic transparent conductor, thereby opening an additional line of prospective applications for the MXenes family. Nevertheless, *GW* and Bethe-Salpeter corrections have a minimal influence on the absorption spectra, in contrast to what is typically observed in semiconductor layers. Our present results suggest that calculations within the independent particle approximation (IPA) calculations are sufficiently accurate for assessing the optical characteristics of bulk-layered MXene materials. Finally, our calculated dielectric properties and absorption spectra, in agreement with existing experimental data, confirm the potential of MXenes as effective infrared emitters.

DOI: 10.1103/PhysRevMaterials.8.075201

I. INTRODUCTION

MXenes, a large family of layered crystals that provide materials engineering with controllable surface functionalization, have been extensively explored for a wide range of technological applications [1–3], including sensors [4–8], energy storage [9–11], generation [12,13], and catalysis [14]. These primarily metallic materials have also proven to be well-suited for electromagnetic interference shielding, and transparent conductive and antireflection coatings [15–21]. Additionally, they show unique optical characteristics such as surface plasmon resonances that enhance absorption in the visible and near-infrared regions. The absorption efficiency depends, however, on their composition and surface functionalization [22,23], as confirmed by calculations at the independent particle level for Ti_2CT_2 and $Ti_3C_2T_2$ crystals [24–26].

The optical response of this extensive family of materials is interesting and can be explored from first-principles calculations. Nonetheless, the precise first-principles optical characterization often requires the use of many-body-perturbation-theory (MBPT) approaches, such as G_0W_0 [27] and the Bethe-Salpeter equation (BSE) [28], which account for electron-electron correlation effects and quasiparticle (QP) energies beyond conventional density functional theory (DFT) calculations. Many-body corrections are known to have a strong influence on both band gap and quasiparticle energies of various layered semiconductors [29–37]. Yet, such corrections have been less explored in metallic layers. This is partially due to the fact that in standard bulk three-dimensional (3D) systems, the metallic screening makes the many-body corrections ineffective, leaving the energy of the quasiparticle states unchanged with respect to the DFT reference values. Moreover, the inclusion of the metallic screening in the framework of MBPT calculations is not straightforward and methodologically challenging.

In fact, an accurate use of the G_0W_0 and BSE approximations in systems with metallic screening requires a good description of the frequency dependency of the polarizability, which may in turn require going beyond the plasmon pole approximation (PPA), significantly enhancing computational cost. Moreover, in metals one needs to account for intraband transitions at long wavelengths, where the intraband contribution to the dielectric function in the $\mathbf{q} \to \mathbf{0}$ limit becomes critical [38–40]. The intraband contribution to the optical transitions is particularly relevant for energies below 1 eV, however this term is often not included in the most common implementations, originally developed for semiconductors. A common approach to include the missing intraband contribution, both at the *GW* and BSE levels, relies on the use of a phenomenological Drude-like term that depends on a plasma frequency ω_D and a damping factor γ [41]. In principle, these parameters can be determined fully *ab initio*, however the computational methods can become computationally expensive [39,41–48]. Alternatively, experimental values can be used when available, which is not the case for the systems under study. There are also some alternative analytical models

*Contact author: claudia.cardoso@nano.cnr.it

†Contact author: cem.sevik@uantwerpen.be

in the literature that avoid explicit Fermi-surface calculations while using a limited number of **k**-points [49–51].

In a recent work, Leon *et al.* [38] tackled this issue by implementing two computationally efficient methods for metals, applied to Al and Na: (i) extrapolating the position of the main pole in the polarizability, from small $\mathbf{q}$ to $\mathbf{q} = 0$, and computing the intraband pole through the f-sum rule, and (ii) approximating the dielectric function at $\mathbf{q} = \mathbf{0}$ by a constant dielectric function determined at small $\mathbf{q}$ values [constant approximation (CA)]. Given the dominant contribution in MXene crystals of the partially filled transition-metal d-shells to the states near the Fermi level [1,52], we will make use of the approaches mentioned above in order to assess the role of intraband transitions in the optical properties.

Taking all these issues into account, we investigated the optical properties of several MXene crystals, specifically Ti_2CCl_2, Ti_2CBr_2, $Ti_3C_2T_2$ (T = F, Cl, Br, S, O, H, and OH), Nb_2CCl_2, and Nb_2CBr_2, that were chosen considering their recently reported successful synthesis [53–55]. We start by systematically investigating the systems with smaller unit cells (Ti_2CCl_2, Ti_2CBr_2, Nb_2CCl_2, and Nb_2CBr_2), calculating the electronic and optical properties at different levels of theory: for the electronic structure we employ (i) G_0W_0 and (ii) G_0W_0 with an intraband correction for the screening, applied using both the Drude approach as implemented in the YAMBO code [56,57] and the CA approximation introduced in Ref. [38]; for the optical properties, we use (iii) BSE and (iv) BSE with an intraband correction for the screening, again using both a Drude correction and CA. Having performed these test calculations, we finally calculate the optical properties of these materials, including both inter- and intraband contributions. We then extend the study to the larger systems, namely $Ti_3C_2T_2$ (T = F, Cl, Br, S, O, H, and OH).

The paper is organized as follows. In Sec. II, we provide the computational details of our approach. In Sec. III, we compare the band structures of the selected bulk-layered materials computed at the DFT and G_0W_0 levels. We analyze the impact of the G_0W_0 correction on the optical properties, the influence of intraband contributions on G_0W_0 and BSE level calculations, and we present the ultimately accurate optical properties. We summarize our results in Sec. IV, offering a concise overview of the methodologies employed to accurately predict the optical properties of multilayered MXene materials.

II. COMPUTATIONAL METHODS

We start by computing the structural and electronic properties of Ti_2CCl_2, Ti_2CBr_2, Nb_2CCl_2, and Nb_2CBr_2 using DFT as implemented in the Quantum ESPRESSO package [58,59]. We employed the generalized gradient approximation (GGA) with Perdew-Burke-Ernzerhof (PBE) exchange-correlation functionals [60,61] and we accounted for the van der Waals (vdW) interactions between layers, using the semiempirical DFT-D2 Grimme method [62]. To include many-body effects, we performed G_0W_0 calculations using the YAMBO code [56,57]. Since the materials under study are metallic, we used a real-axis frequency grid with 100 points in the descriptions of the dynamical electronic screening (tests up to 200 frequency points showed QP variations typically of the order of a few meV). The BSE [28] was then solved on top of both PBE and G_0W_0 results to assess the influence of quasiparticle interactions on the optical properties of these bulk materials. The energy cutoff for the G-vectors used in the sum of the exchange self-energy and the density was set to 40 Ry. The energy cutoff for the response function was chosen as 7 Ry, both for the dynamically and statically screened interactions.

At the BSE level, the energy cutoff for the wave function (FFTGvecs) was set to 40 Ry. When reporting the quasiparticle energies for the bulk materials, we employed a Γ-centered $24 \times 24 \times 6$ k-grid mesh, which corresponds to 340 k-points in the irreducible Brillouin zone, summing over 400 states for both the screening function and the Green's function. The optical spectra of these materials were obtained by considering the first 15 000 excitonic states using the SLEPC library [63].

Providing an accurate account of the computational cost of these calculations is not straightforward, since it depends strongly on the computational architecture used. In the present case, a calculations within the independent particle approximation (IPA) calculation took a couple of hours in a single state-of-the-art computational node (2 × AMD Epyc 7452, with 32 cores). In contrast, the GW or BSE calculations can take more than 4 days in eight nodes of the same type. This is due in part to the large memory requirements of the calculations, which do not allow to take advantage of all the processors in each node. For example, the GW calculation for Nb_2CCl_2 in a CPU-only cluster (2 × AMD Epyc 7452, with 32 cores) with eight nodes took around 72 h.

When the intraband corrections to the screening were done within the Drude model, we used the free-electron plasma model with the expression

$$\varepsilon^{\text{intra}}(\omega) = 1 - \frac{\omega_p^2}{\omega^2 + \gamma^2} + i\frac{\omega_p^2 \gamma}{\omega(\omega^2 + \gamma^2)}, \tag{1}$$

The plasma frequency, ω_p and the damping factor γ values were estimated by fitting Eq. (1) to the independent-particle optical spectra ε_1 and ε_2, computed using the YAMBO code, for $\mathbf{q} \sim \mathbf{0}$ from which we subtract $\varepsilon_2(\mathbf{q} = \mathbf{0})$, where only the interband part is present. The selected $\mathbf{q} \sim \mathbf{0}$ point lays in the x-y plane, where the k grid is denser due to the layered character of the systems under study. More details and the final fitting results are shown in Figs. S2–S4 of the Supplemental Material (SM) [64].

The intraband corrections are included in the calculation essentially at two different stages. The first stage is when calculating the polarizability χ and the static screened potential W, respectively, for the GW and the BSE calculations, either using the Drude model or CA. The main difference between the two models is that the Drude correction addresses only the head matrix element of the polarizability ($\mathbf{G} = \mathbf{G}' = 0$), whereas CA corrects all χ matrix elements. A second correction is done after the BSE calculations, at which an intraband Drude term for $\mathbf{q} = \mathbf{0}$ is added to the computed dielectric function.

The optical absorption spectra are obtained through the complex dielectric function $\varepsilon(\omega) = \varepsilon_1(\omega) + i\varepsilon_2(\omega)$, with the absorption coefficient $I(\omega)$ given by the following expression [65,66]:

$$I(\omega) = \sqrt{2}\omega\left(\sqrt{\varepsilon_1^2(\omega) + \varepsilon_2^2(\omega)} - \varepsilon_1(\omega)\right)^{1/2}. \tag{2}$$

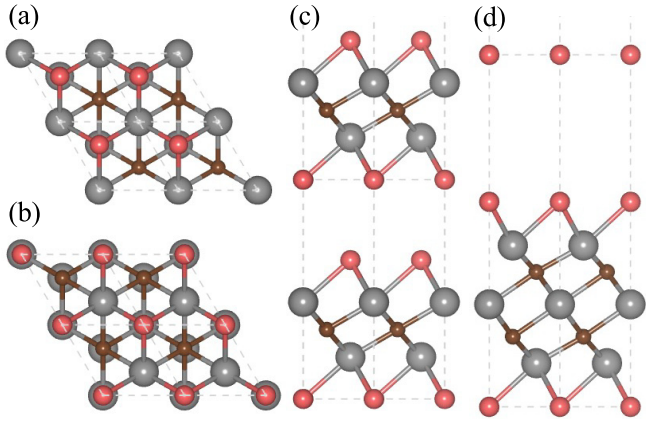

FIG. 1. Top and side views of the optimized crystal structures of (a)–(c) M_2CT_2 (M = Ti, Nb; T = Cl, Br) and (b)–(d) $Ti_3C_2T_2$ (T = F, Cl, Br, S, O, H, and OH). A 2 × 2 supercell is displayed for clarity. Gray spheres represent titanium or niobium atoms, while brown and red spheres represent carbon and surface layer atoms, respectively.

The normalization is computed as follows:

$$100 \times [1 - \exp(-I(\omega) \times \Delta t)], \tag{3}$$

where Δt represents the thickness of the material, which in our study is taken as 100 nm.

III. RESULTS AND DISCUSSION

A. Electronic properties

The bulk MXene crystals considered, with two and three metal layers in their unit cells, exhibit a hexagonal, layered lattice structure, as presented in Fig. 1. We optimized the crystal structures, obtaining ground-state lattice parameters that are in good agreement with previous reports [53,67,68] and reported in the SM [64]. We then computed the electronic band structures of the MXenes with two metal layers at the vdW-corrected DFT/PBE and G_0W_0 levels of theory. The results, depicted in Fig. 2, reveal the metallic nature of these crystals.

The overall influence of G_0W_0 correction in the band structure is small, but there are some energy regions with more

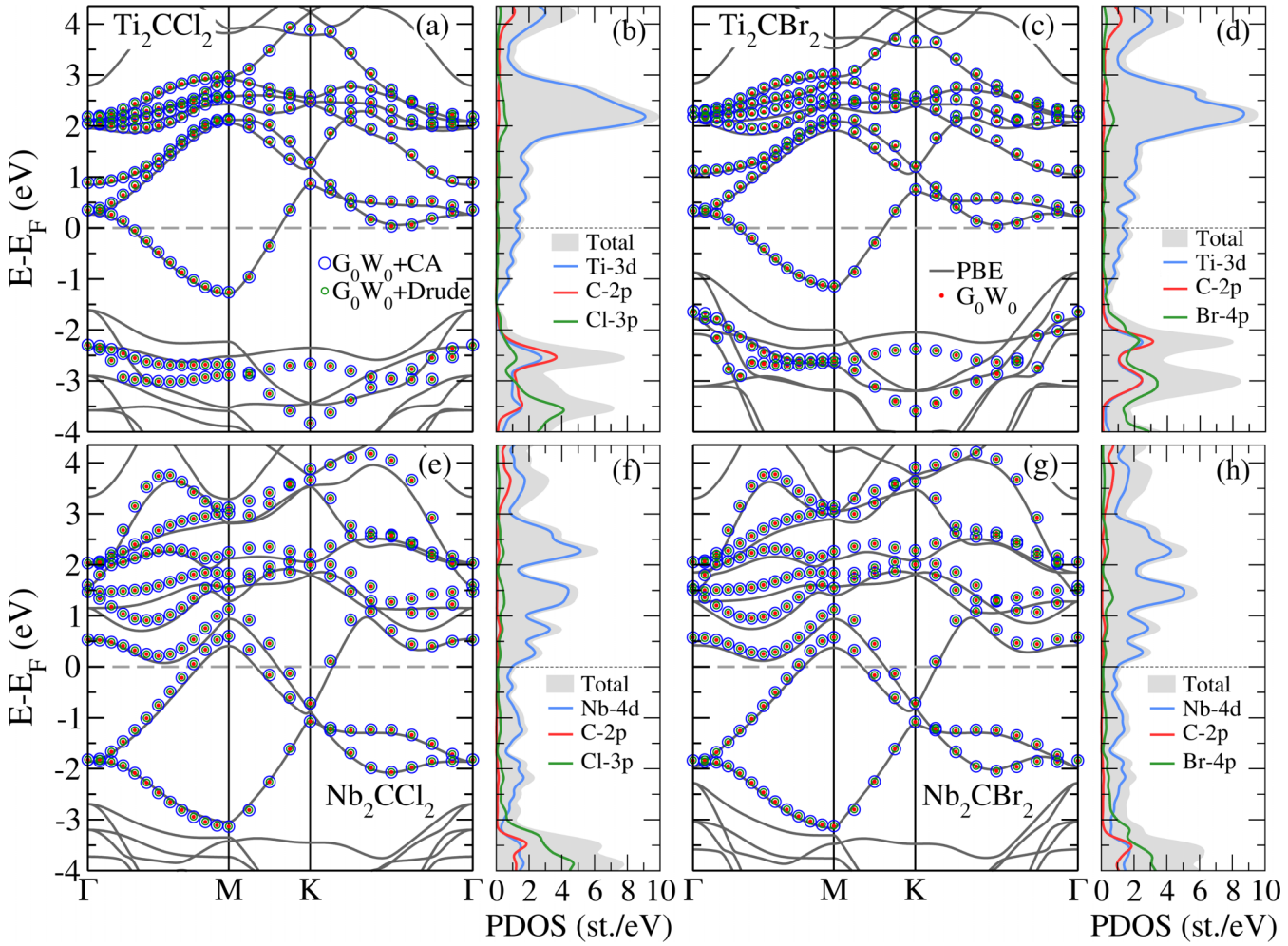

FIG. 2. Comparison between the PBE, G_0W_0, G_0W_0 + CA, and G_0W_0 + Drude band structures of bulk-layered MXenes, and their total and projected density of states computed within PBE: (a) and (b) for Ti_2CCl_2, (c) and (d) for Ti_2CBr_2, (e) and (f) for Nb_2CCl_2, (g) and (h) for Nb_2CBr_2. The gray-solid, red-dotted, blue-circle, and green-circle lines represent PBE, G_0W_0, G_0W_0 + CA, and G_0W_0 + Drude band structures, respectively. The gray shadow, blue, red, and green lines represent total, Ti(Nb)-*d*, C-*p*, and Cl(Br)-*p* orbitals, respectively. The Fermi level corresponds to 0 eV.

significant corrections, with interesting consequences. For the compounds with Ti, the largest corrections, ∼0.4 eV, are seen for the energy range from – 4 to – 2 eV around the *K* point. For Ti_2CCl_2 (Ti_2CBr_2) in this energy region, the Ti-3*d*, C-2*p*, and Cl-3*p* (Br-4*p*) orbitals are strongly hybridized, as shown by the projected density of states (PDOS) plotted in the Figs. 2(b) and 2(d). It is interesting to note that the resulting band structure closely resembles the type 3 intrinsic transparent conductors described in Ref. [69], with the partially filled band separated from the band below by a considerable energy gap. In fact, these systems present all the properties of typical transparent conductive materials, with the notable difference of being intrinsic, and not obtained through the doping of a wide-band-gap semiconductor.

In contrast, for Nb_2CCl_2 and Nb_2CBr_2, the Nb-4*d* orbitals, in the same energy region, present a weaker hybridization that result in much smaller G_0W_0 corrections. On the other hand, from 3 to 4 eV above the Fermi energy, the Nb systems show hybridization between the Nb-4*d* and the C-2*p* states [Figs. 2(f) and 2(h)] with *GW* corrections of about 0.38 eV for Nb_2CCl_2 along *K*-Γ and 0.19 eV for Nb_2CBr_2 along *M*-*K*. Around the Γ point, the bands 1.5 eV above the Fermi level, where Nb-4*d* and the *p* states of either Cl or Br mix, show again corrections of 0.32 and 0.22 eV. The G_0W_0 corrections seem to be more relevant for strongly hybridized states.

The results including the intraband contribution to the dielectric function in the $\mathbf{q} \to \mathbf{0}$ limit, calculated within both Drude (G_0W_0 + Drude) and CA (G_0W_0 + CA) approximations, are shown in Fig. 2. The different band structures are in practice indistinguishable, demonstrating that the intraband corrections at the G_0W_0 level are negligible and can thus be neglected.

B. Optical properties

1. The influence of G_0W_0 and BSE corrections

Since the systems under study are layered materials, we will focus on the in-plane components of the dielectric function. Figure 3 shows the imaginary part of the in-plane dielectric functions, $\varepsilon_2^{\text{inter}}$, and the optical absorption spectrum, $I(\omega)$, computed within the independent particle approximation (IPA) and the Bethe-Salpeter equation (BSE) on top of both PBE and G_0W_0 calculations. The IPA and the BSE results are fairly similar. The differences seen above 2 eV are due to the number of bands included in the BSE calculation, which are not enough to describe the spectra at higher energies.

On the other hand, the G_0W_0 energy corrections lead to some differences on $\varepsilon_2^{\text{inter}}$ that are particularly evident in Ti-based structures, for which the QP corrections are larger. In fact, the dielectric function of Ti_2CCl_2 at the *GW* level presents an extra peak below 0.2 eV. In general, the peaks present between 0 and 1 eV, both for Ti and Nb compounds, are shifted about 0.1 eV higher in energy in the case of *GW* with respect to the PBE value, consistent with the negative (positive) *GW* energy correction of the occupied (empty) states.

Despite these differences on the $\varepsilon_2^{\text{inter}}$ curves, their impact on the final optical absorption spectra is less visible, and in fact the $I(\omega)$ curves computed starting from PBE and *GW* band structures are fairly similar. Considering the

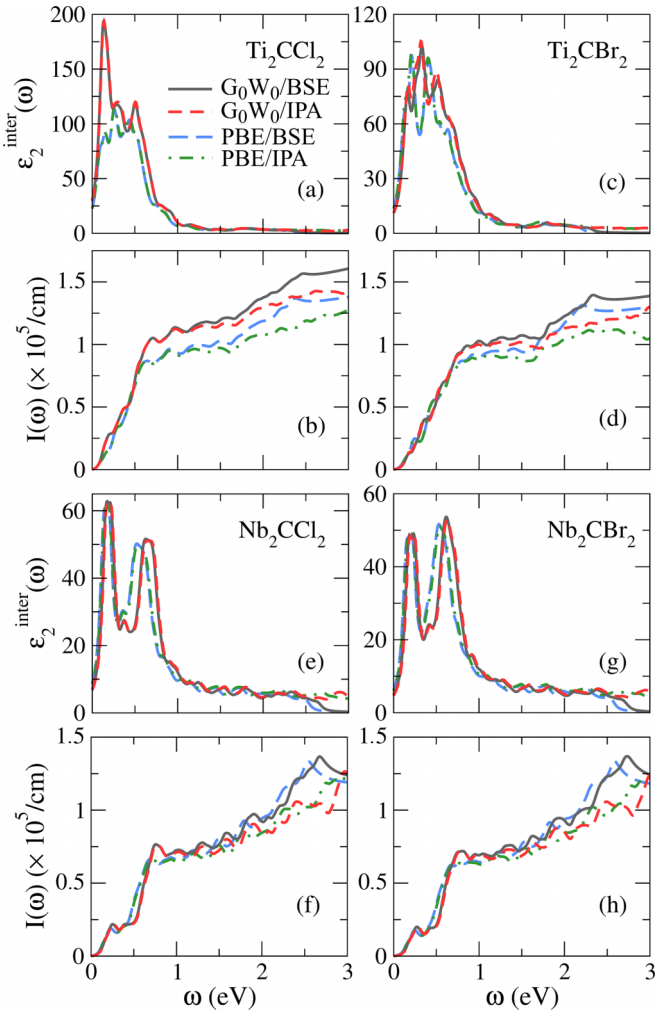

FIG. 3. Imaginary parts of the in-plane dielectric functions and the absorption coefficients of bulk-layered MXenes: (a) and (b) for Ti_2CCl_2, (c) and (d) for Ti_2CBr_2, (e) and (f) for Nb_2CCl_2, (g) and (h) for Nb_2CBr_2. The gray solid, red short-dashed, blue long-dashed, and green dot-dashed lines represent the results of G_0W_0/BSE, G_0W_0/IPA, PBE/BSE, and PBE/IPA, respectively.

computational cost of the G_0W_0 corrections, it seems reasonable to neglect them in the calculation of the optical absorption of the MXene family, which is an important advantage for, e.g., high-throughput analysis or other automated studies. The calculated ε_1 results, presented in Fig. S5 in the SM [64], confirm this conclusion.

2. The influence of intraband correction on G_0W_0 and BSE levels

Following the assessment of the influence of *GW* and BSE corrections on electronic energies, quasiparticle energies, and optical properties, we now investigate the impact of intraband transitions on the BSE calculations. In this study, we adopted two distinct approaches to correct the polarizability or, more precisely, its product with the Coulomb potential $Y = v\chi$, as detailed in Ref. [38]: (i) we added a complex Drude pole expressed as $Y_D(\omega) = \omega_D^2[\omega(\omega + i\gamma)]^{-1}$, and (ii) we approximated the full $Y(\mathbf{q} = \mathbf{0})$ matrix element by its nearest neighbor, $Y(\mathbf{q} \neq \mathbf{0})$, i.e., with the *q*-vector closest to

TABLE I. The fitting values of plasma frequencies (ω_p) and damping parameters (γ) of all the considered materials.

Systems	ω_p^2 (eV^2)	γ(eV)	Systems	ω_p^2 (eV^2)	γ(eV)
Ti_2CCl_2	12.4	0.157	$Ti_3C_2F_2$	26.5	0.141
Ti_2CBr_2	10.1	0.180	$Ti_3C_2Cl_2$	16.4	0.158
			$Ti_3C_2Br_2$	10.7	0.183
			$Ti_3C_2O_2$	9.6	0.160
Nb_2CCl_2	21.2	0.166	$Ti_3C_2S_2$	14.5	0.147
Nb_2CBr_2	23.4	0.163	$Ti_3C_2H_2$	9.7	0.134
			$Ti_3C_2(OH)_2$	16.0	0.200

0 according to the adopted k-point grid. Here, the Drude pole was determined as explained in Sec. II. The obtained ω_p^2 and γ values are listed in Table I.

The calculated in-plane $\varepsilon_2^{\text{inter}}$ is shown in Fig. 4 for five different calculations, the first without intraband corrections for $\mathbf{q} = \mathbf{0}$ and the other four with intraband corrections either at the GW or the BSE level: (i) G_0W_0/BSE corresponds to BSE calculations on top of G_0W_0 results without any intraband correction for $\mathbf{q} = \mathbf{0}$; (ii) G_0W_0 + CA/BSE and (iii) G_0W_0 + Drude/BSE correspond to BSE calculations on top of G_0W_0 results corrected either with CA or the Drude model; (iv) G_0W_0/BSE + CA and (v) G_0W_0/BSE + Drude refer to BSE calculations on top of G_0W_0 results with a CA or Drude correction at the BSE level. It is worth noticing that the corrections are included in the screened potential W, but the final BSE spectra at this point still do not include the intraband contribution in the long-wavelength limit $\mathbf{q} = \mathbf{0}$, which justifies the label $\varepsilon^{\text{inter}}$. These will be discussed in Sec. III C.

Since the GW quasiparticle corrections are similar when computed using a polarizability with and without intraband

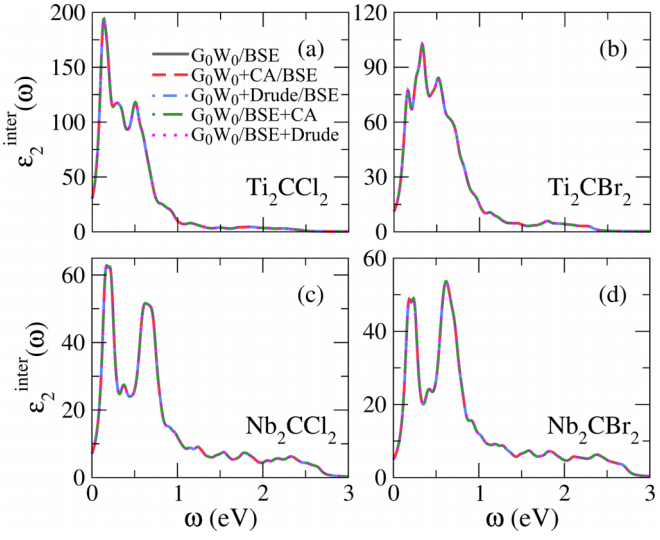

FIG. 4. Imaginary parts of the in-plane dielectric functions of bulk-layered MXenes: (a) for Ti_2CCl_2, (b) for Ti_2CBr_2, (c) for Nb_2CCl_2, (d) for Nb_2CBr_2. The gray solid, red dashed, blue dot-short-dashed, green dot-long-dashed, and magenta dotted lines represent the results of G_0W_0/BSE, G_0W_0 + CA/BSE, G_0W_0 + Drude/BSE, G_0W_0/BSE + CA, and G_0W_0/BSE + Drude, respectively.

corrections, as described above and illustrated in Fig. 2, as expected, the BSE spectra computed on top of these three calculations are also similar. The intraband correction of W at the BSE level also has no visible effect. In fact, these results suggest that the intraband correction to the response function is not essential for the calculation of the optical properties of layered MXene structures and will be neglected for the remaining systems.

C. Dielectric properties

After assessing the effect of the intraband correction on the screened potential of the metallic materials under study, we finally compute the optical properties using G_0W_0/BSE methods including also intraband excitations. In line with previous analysis, the intraband transitions were included employing the Drude model as described in the Methods section. The values determined for ω_p^2 and γ are listed in Table I and the figures depicting the accuracy of the fitting are presented in the SM [64]. Using the computed Drude parameters, we then add to the BSE spectra the intraband contribution given by Eq. (1).

Figure 5 presents the real (ε_1) and the imaginary (ε_2) parts of the dielectric functions derived from these calculations. In the 0–1 eV range, substantial contributions both from intra- and interband transitions can be seen for all materials, indicating a region with a high potential for optical response. The most intense peaks in the interband spectrum are below 1 eV and can be identified with transitions between states close to the Fermi level in the Γ-M region, as illustrated by the band structures shown in Fig. 2. The ε_2 spectra here obtained are in good agreement with the spectra of (i) F and OH terminated Ti_2CT_2 and $Ti_3C_2T_2$ MXenes, estimated by the HSE06 and Drude approximations [25] and (ii) F, Cl, Br, and I terminated $Ti_3C_2T_2$ MXenes obtained via DFT calculations [70].

The real components of the intra- and interband spectra in this energy range are very different, unequivocally indicating the need to include intraband transitions when computing the dielectric functions of these materials. The present analyses reveal that the materials under study display a region with a negative real dielectric function, hinting at their prospective utility in surface plasmon applications [71]. In fact, the real components of the dielectric function are comparable with those of Al, Cu, and Ag [72]. However, their imaginary part, particularly in the 0–1 eV interval, are more pronounced than those of standard metals, due to the presence of carbon and chlorine or boron atoms alongside the transition-metal atom in MXenes.

The absorption capacity is the ability of a material to absorb electromagnetic radiation, and it depends on the wavelength. The absorption spectra, computed within BSE, are shown in Fig. 6. As the wavelength (λ) increases, there is a monotonic decrease in both the inter (α_{inter}) and the total, i.e., inter + intra (α) contributions. The absorption reaches a maximum value ranging from 70% to 80% in the ultraviolet region, indicative of a metallic character [73]. Notably, responses exceeding 50% are also observed in the infrared region. The vertical axis on the right-hand side of Fig. 6, colored in blue, quantifies the contribution of the intraband transitions to the spectra ($100\,[\alpha - \alpha_{\text{inter}}]/\alpha$). As anticipated,

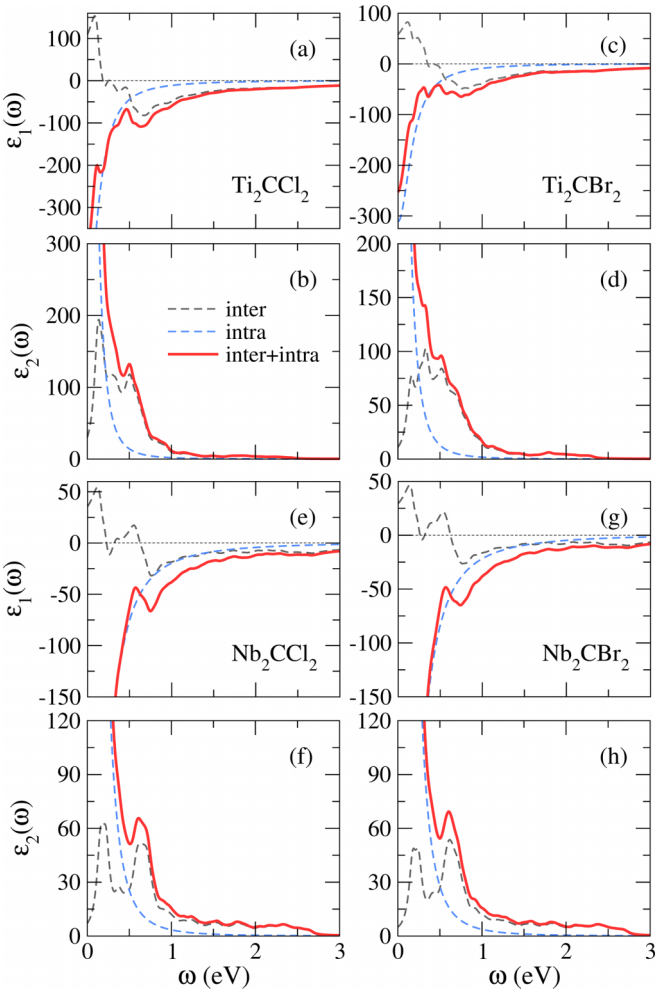

FIG. 5. Real and imaginary parts of the dielectric function of bulk-layered MXenes calculated with G_0W_0/BSE: (a) and (b) for Ti_2CCl_2, (c) and (d) for Ti_2CBr_2, (e) and (f) for Nb_2CCl_2, (g) and (h) for Nb_2CBr_2. The gray dashed, blue dashed, and red solid lines represent inter, intra, and inter + intra contributions, respectively.

this contribution is below 5% at lower wavelengths but increases to approximately 20% at higher wavelengths, showing the relevance of the $\mathbf{q} = \mathbf{0}$ intraband transitions in the determination of a material's absorption properties.

D. The $Ti_3C_2T_2$ compounds

We now extend our study to the MXene compounds $Ti_3C_2T_2$ (T = F, Cl, Br, S, O, H, and OH). As described previously, these compounds feature three metal layers, with seven atoms in each unit cell. A schematic crystal representation and the corresponding lattice constants are presented in Fig. S1 and Table S1 of the SM [64]. The number of atoms in their unit cells makes these compounds computationally more challenging than the M_2CT_2 class, particularly when performing *GW* calculations. In Fig. 7 we present the band structure and the PDOS computed for $Ti_3C_2Cl_2$ and $Ti_3C_2Br_2$ within PBE. We show also the *GW* corrected band structures. We report, in the SM [64], the bands calculated for the remaining systems at the PBE level, and in some cases also the *GW* results obtained

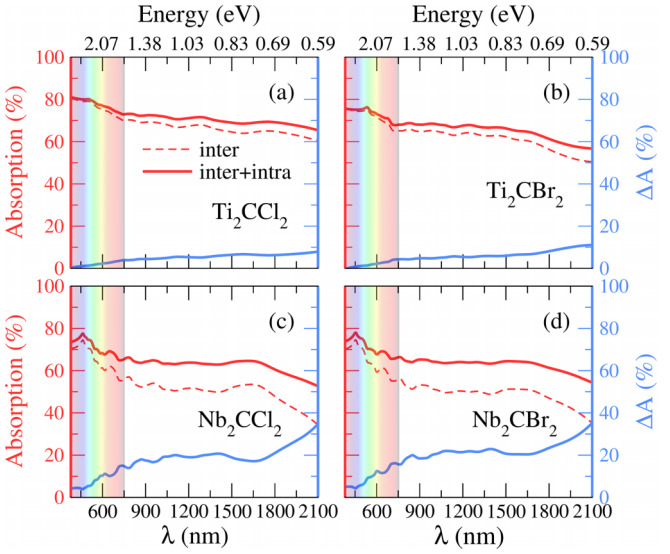

FIG. 6. The normalization of absorption coefficient of bulk-layered MXenes calculated with G_0W_0/BSE via Eq. (2): (a) for Ti_2CCl_2, (b) for Ti_2CBr_2, (c) for Nb_2CCl_2, and (d) for Nb_2CBr_2. The dashed and solid red lines represent inter and inter + intra contributions, respectively. The blue line shows the change when intraband transitions are not considered.

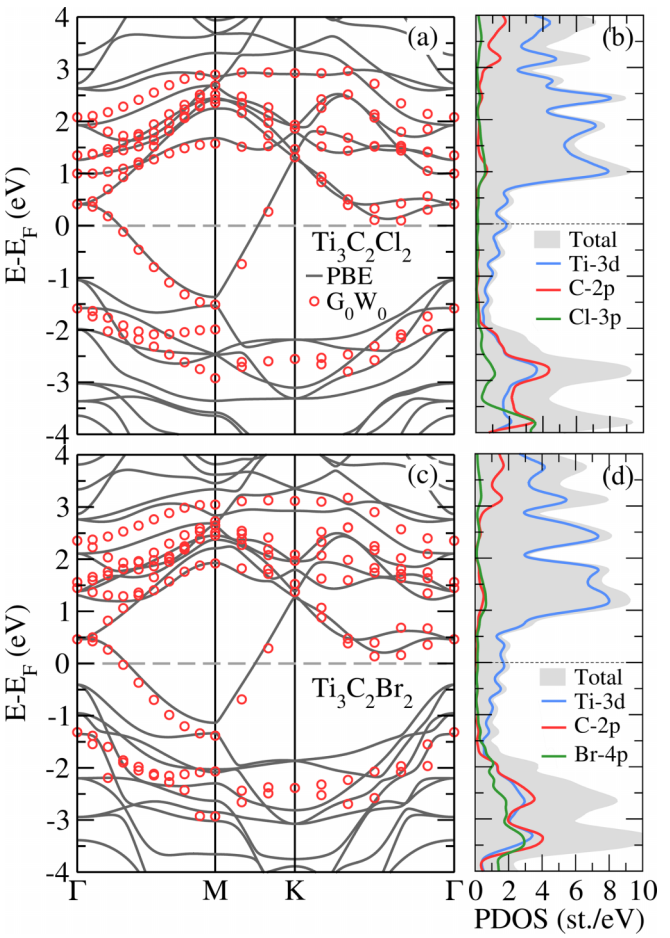

FIG. 7. Band structure computed within PBE and G_0W_0, and PDOS computed within PBE of bulk-layered MXenes: (a) and (b) for $Ti_3C_2Cl_2$, (c) and (d) for $Ti_3C_2Br_2$.

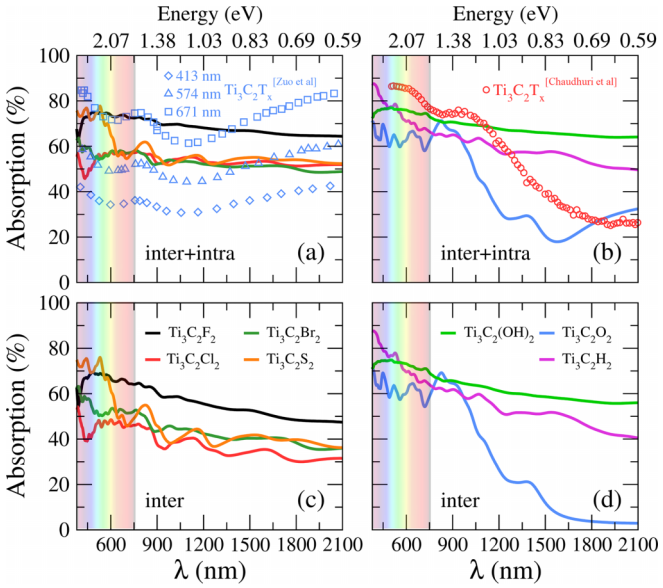

FIG. 8. The normalization of absorption coefficient of bulk-layered $Ti_3C_2T_2$ MXenes calculated with PBE/IPA via Eq. (2) (a) for inter + intra contribution and (b) for inter contribution, compared with the experimental results of $Ti_3C_2T_x$ from Zuo *et al.* [75] and Chaudhuri *et al.* [74]. The black, red, dark-green, blue, orange, magenta and light-green lines show the results for $Ti_3C_2F_2$, $Ti_3C_2Cl_2$, $Ti_3C_2Br_2$, $Ti_3C_2O_2$, $Ti_3C_2S_2$, $Ti_3C_2H_2$, and $Ti_3C_2(OH)_2$, respectively.

with unconverged k-grids, in order to illustrate the qualitative effect of these corrections.

Again the calculations show larger GW correction in the regions were d and p states coexist. If we compare the band structures of $Ti_3C_2Cl_2$ and $Ti_3C_2Br_2$ with Ti_2CCl_2 and Ti_2CBr_2 discussed in the previous sections, the most obvious difference is the smaller energy gap along Γ-M between the occupied d and p states in the case of the three-metal-layer systems.

Our analysis of the optical response of the M_2CT_2 (M = Ti, Nb; T = Cl, Br) systems done above shows that their electronic properties computed at the PBE and GW level, and their optical properties computed at the IPA and BSE levels, are not significantly different. On the other hand, it is important to consider the intraband contribution to the spectra, done here through a Drude model parametrization. With this assumption, we have computed the optical properties of additional MXene materials by performing IPA calculations on top of PBE band structures, and then we corrected for the intraband transition within the Drude model. The parameters of the model are listed in Table I. The calculated electronic band structures and projected density of states, as well as the real/imaginary parts of the dielectric constants for these materials, are illustrated in Figs. S6-S7 and Figs. S8-S9 in the SM [64], respectively. We used the same computational settings for the plane-wave energy cutoff, k-point grid, and vdW correction across these materials.

The inter and inter + intra absorption spectra, computed using PBE/IPA, are presented in Fig. 8. The inclusion of the intraband contributions makes the spectra of several MXenes similar, particularly in the higher wavelength range, with the exception of $Ti_3C_2O_2$. In fact $Ti_3C_2F_2$ and $Ti_3C_2(OH)_2$ almost coincide. Among the considered materials, $Ti_3C_2H_2$ exhibits maximum absorbance around the UV region, while $Ti_3C_2F_2$ and $Ti_3C_2(OH)_2$ show a wide spectrum of maximum absorbance within the range of 70–80%. The Cl, Br, S, and H functionalized structures display comparable absorption spectra for wavelengths >1000 nm. The spectra intensity of $Ti_3C_2Cl_2$ and $Ti_3C_2Br_2$ are slightly lower than the intensities computed for the corresponding two-layer systems, Ti_2CCl_2 and Ti_2CBr_2 shown above.

The present results agree qualitatively with experimental measurements available for $Ti_3C_2T_x$ MXene and included in Fig. 8 for reference, suggesting similar absorption potential in both infrared and ultraviolet regions [74–77]. O-functionalized Ti_3C_2 differs from the other compounds, particularly the F, OH, and H cases, showing a significant decrease in the absorption with increasing wavelengths. Notably, this echoes the experimental measurements reported for randomly functionalized Ti_3C_2 [74] which leads us to speculate about a possible dense O functionalization in the reported experiment.

IV. SUMMARY AND CONCLUSIONS

We have performed detailed electronic and optical first-principles calculations for a selected group of metallic MXene bulk-layered crystals, focusing on the effect of many-body corrections and the inclusion of intraband corrections on the optical properties of those materials. Our results show that the GW corrections to the band structure are not uniform in the energy range, being larger in the regions with larger hybridization between p-d states. The present results reveal that, at least for Ti_2CCl_2, the GW corrections can open a gap between the occupied states, resulting in a band structure typical of intrinsic transparent conductors, which opens a novel prospective field of applications for the MXenes family, and they will be explored in future research. We find that the intraband contribution to the response function is negligible and can be omitted.

We subsequently computed the optical properties of the same selected systems at IPA and BSE levels. Interestingly, the GW corrections do not lead to significant differences on the final absorption spectra. This suggests that, for systems within the MXenes family, the absorption spectra can be computed on top of Kohn-Sham eigenvalues without a significant loss of accuracy. Again, excitonic corrections seem to exert almost a negligible influence on the resulting dielectric properties, suggesting that an IPA calculation already yields sufficiently accurate optical spectra.

It is crucial, however, to recognize that the contributions of the intraband transitions to the final absorption profile may be as high as 20% and should therefore be included. In the present work, we have modeled the intraband contribution using the Drude model, whose parameters were determined with a method that does not take any toll on the computational cost, being therefore conveniently suited for the calculation of the optical spectra for large metal systems, such as the MXene multilayers.

ACKNOWLEDGMENTS

The following computational resources and services were used in this work: The VSC (Flemish Supercomputer Center), funded by the Research Foundation Flanders (FWO) and the Flemish Government - department EWI; TRUBA, High Performance and Grid Computing Center, funded by the Scientific and Technological Research Council of Turkey (TUBITAK); and UHeM, National Center for High Performance Computing of Turkey under Grants No. 1007502020 and No. 5016212023. Z.K. acknowledges financial support from TUBITAK 2218-National Postdoctoral Research Fellowship Program under Project No. 118C570.

[1] K. Hantanasirisakul and Y. Gogotsi, Electronic and optical properties of 2D transition metal carbides and nitrides (MXenes), Adv. Mater. **30**, 1804779 (2018).

[2] Y. Gogotsi and B. Anasori, The rise of MXenes, ACS Nano **13**, 8491 (2019).

[3] X. Li, Z. Huang, C. E. Shuck, G. Liang, Y. Gogotsi, and C. Zhi, MXene chemistry, electrochemistry and energy storage applications, Nat. Rev. Chem. **6**, 389 (2022).

[4] S. H. Lee, W. Eom, H. Shin, R. B. Ambade, J. H. Bang, H. W. Kim, and T. H. Han, Room-temperature, highly durable $Ti_3C_2T_x$ MXene/graphene hybrid fibers for NH_3 gas sensing, ACS Appl. Mater. Interfaces **12**, 10434 (2020).

[5] Y. Ma, N. Liu, L. Li, X. Hu, Z. Zou, J. Wang, S. Luo, and Y. Gao, A highly flexible and sensitive piezoresistive sensor based on MXene with greatly changed interlayer distances, Nat. Commun. **8**, 1207 (2017).

[6] Y. Cai, J. Shen, G. Ge, Y. Zhang, W. Jin, W. Huang, J. Shao, J. Yang, and X. Dong, Stretchable $Ti_3C_2T_x$ MXene/carbon nanotube composite based strain sensor with ultrahigh sensitivity and tunable sensing range, ACS Nano **12**, 56 (2018).

[7] Y.-Z. Zhang, K. H. Lee, D. H. Anjum, R. Sougrat, Q. Jiang, H. Kim, and H. N. Alshareef, MXenes stretch hydrogel sensor performance to new limits, Sci. Adv. **4**, eaat0098 (2018).

[8] M. Khazaei, V. Wang, C. Sevik, A. Ranjbar, M. Arai, and S. Yunoki, Electronic structures of imax phases and their two-dimensional derivatives: A family of piezoelectric materials, Phys. Rev. Mater. **2**, 074002 (2018).

[9] B. Anasori, M. R. Lukatskaya, and Y. Gogotsi, 2D metal carbides and nitrides (MXenes) for energy storage, Nat. Rev. Mater. **2**, 16098 (2017).

[10] J. Pang, R. G. Mendes, A. Bachmatiuk, L. Zhao, H. Q. Ta, T. Gemming, H. Liu, Z. Liu, and M. H. Rummeli, Applications of 2D MXenes in energy conversion and storage systems, Chem. Soc. Rev. **48**, 72 (2019).

[11] J. Nan, X. Guo, J. Xiao, X. Li, W. Chen, W. Wu, H. Liu, Y. Wang, M. Wu, and G. Wang, Nanoengineering of 2D MXene-based materials for energy storage applications, Small **17**, 1902085 (2021).

[12] C. Yang, H. Huang, H. He, L. Yang, Q. Jiang, and W. Li, Recent advances in MXene-based nanoarchitectures as electrode materials for future energy generation and conversion applications, Coord. Chem. Rev. **435**, 213806 (2021).

[13] H. T. Das, T. E. Balaji, S. Dutta, N. Das, and T. Maiyalagan, Recent advances in MXene as electrocatalysts for sustainable energy generation: A review on surface engineering and compositing of MXene, Int. J. Energy Res. **46**, 8625 (2022).

[14] T. P. Nguyen, D. M. Tuan Nguyen, D. L. Tran, H. K. Le, D.-V. N. Vo, S. S. Lam, R. S. Varma, M. Shokouhimehr, C. C. Nguyen, and Q. V. Le, MXenes: Applications in electrocatalytic, photocatalytic hydrogen evolution reaction and CO_2 reduction, Mol. Catal. **486**, 110850 (2020).

[15] F. Shahzad, M. Alhabeb, C. B. Hatter, B. Anasori, S. M. Hong, C. M. Koo, and Y. Gogotsi, Electromagnetic interference shielding with 2D transition metal carbides (MXenes), Science **353**, 1137 (2016).

[16] K. Hantanasirisakul, M.-Q. Zhao, P. Urbankowski, J. Halim, B. Anasori, S. Kota, C. E. Ren, M. W. Barsoum, and Y. Gogotsi, Fabrication of $Ti_3C_2T_x$ mxene transparent thin films with tunable optoelectronic properties, Adv. Electron. Mater. **2**, 1600050 (2016).

[17] M. Han, C. E. Shuck, R. Rakhmanov, D. Parchment, B. Anasori, C. M. Koo, G. Friedman, and Y. Gogotsi, Beyond $Ti_3C_2T_x$: MXenes for electromagnetic interference shielding, ACS Nano **14**, 5008 (2020).

[18] B. Zhou, M. Su, D. Yang, G. Han, Y. Feng, B. Wang, J. Ma, J. Ma, C. Liu, and C. Shen, Flexible MXene/silver nanowire-based transparent conductive film with electromagnetic interference shielding and electro-photo-thermal performance, ACS Appl. Mater. Interfaces **12**, 40859 (2020).

[19] Z. Wang, P. Wang, W. Cao, C. Sun, Z. Song, D. Ji, L. Yang, J. Han, and J. Zhu, Robust, transparent, and conductive AgNW/MXene composite polyurethane self-healing film for electromagnetic interference shielding, J. Mater. Chem. C **10**, 17066 (2022).

[20] R. Rakhmanov, C. E. Shuck, J. Al Hourani, S. Ippolito, Y. Gogotsi, and G. Friedman, Ultrathin MXene film interaction with electromagnetic radiation in the microwave range, Appl. Phys. Lett. **123**, 204105 (2023).

[21] M. Han and Y. Gogotsi, Perspectives for electromagnetic radiation protection with MXenes, Carbon **204**, 17 (2023).

[22] L. Wu, Q. You, Y. Shan, S. Gan, Y. Zhao, X. Dai, and Y. Xiang, Few-layer $Ti_3C_2T_x$ MXene: A promising surface plasmon resonance biosensing material to enhance the sensitivity, Sens. Actuators, B **277**, 210 (2018).

[23] D. Wang, Y. Fang, W. Yu, L. Wang, H. Xie, and Y. Yue, Significant solar energy absorption of MXene $Ti_3C_2T_x$ nanofluids via localized surface plasmon resonance, Sol. Energy Mater. Sol. Cells **220**, 110850 (2021).

[24] H. Lashgari, M. Abolhassani, A. Boochani, S. Elahi, and J. Khodadadi, Electronic and optical properties of 2D graphene-like compounds titanium carbides and nitrides: DFT calculations, Solid State Commun. **195**, 61 (2014).

[25] Y. Bai, K. Zhou, N. Srikanth, J. H. L. Pang, X. He, and R. Wang, Dependence of elastic and optical properties on surface terminated groups in two-dimensional MXene monolayers: A first-principles study, RSC Adv. **6**, 35731 (2016).

[26] T. Bashir, S. A. Ismail, J. Wang, W. Zhu, J. Zhao, and L. Gao, MXene terminating groups O,–F or–OH,–F or O,–OH,–F, or O,–OH,–Cl? J. Energy Chem. **76**, 90 (2023).

[27] M. S. Hybertsen and S. G. Louie, Electron correlation in semiconductors and insulators: Band gaps and quasiparticle energies, Phys. Rev. B **34**, 5390 (1986).

[28] E. E. Salpeter and H. A. Bethe, A relativistic equation for bound-state problems, Phys. Rev. **84**, 1232 (1951).

[29] P. E. Trevisanutto, M. Holzmann, M. Côté, and V. Olevano, *Ab initio* high-energy excitonic effects in graphite and graphene, Phys. Rev. B **81**, 121405(R) (2010).

[30] T. Cheiwchanchamnangij and W. R. L. Lambrecht, Quasiparticle band structure calculation of monolayer, bilayer, and bulk MoS_2, Phys. Rev. B **85**, 205302 (2012).

[31] H.-P. Komsa and A. V. Krasheninnikov, Effects of confinement and environment on the electronic structure and exciton binding energy of MoS_2 from first principles, Phys. Rev. B **86**, 241201(R) (2012).

[32] A. Molina-Sánchez, D. Sangalli, K. Hummer, A. Marini, and L. Wirtz, Effect of spin-orbit interaction on the optical spectra of single-layer, double-layer, and bulk MoS_2, Phys. Rev. B **88**, 045412 (2013).

[33] C. Espejo, T. Rangel, A. H. Romero, X. Gonze, and G.-M. Rignanese, Band structure tunability in MoS_2 under interlayer compression: A DFT and *GW* study, Phys. Rev. B **87**, 245114 (2013).

[34] M. G. Menezes, R. B. Capaz, and S. G. Louie, *Ab initio* quasiparticle band structure of ABA and ABC-stacked graphene trilayers, Phys. Rev. B **89**, 035431 (2014).

[35] H.-G. Kim and H. J. Choi, Thickness dependence of work function, ionization energy, and electron affinity of Mo and W dichalcogenides from DFT and GW calculations, Phys. Rev. B **103**, 085404 (2021).

[36] D. Amblard, G. D'Avino, I. Duchemin, and X. Blase, Universal polarization energies for defects in monolayer, surface, and bulk hexagonal boron nitride: A finite-size fragments *GW* approach, Phys. Rev. Mater. **6**, 064008 (2022).

[37] E. Jung, J. C. Park, Y.-S. Seo, J.-H. Kim, J. Hwang, and Y. H. Lee, Unusually large exciton binding energy in multilayered 2H-$MoTe_2$, Sci. Rep. **12**, 4543 (2022).

[38] D. A. Leon, A. Ferretti, D. Varsano, E. Molinari, and C. Cardoso, Efficient full frequency GW for metals using a multipole approach for the dielectric screening, Phys. Rev. B **107**, 155130 (2023).

[39] A. Marini, G. Onida, and R. Del Sole, Quasiparticle electronic structure of copper in the *GW* approximation, Phys. Rev. Lett. **88**, 016403 (2001).

[40] K. Kolwas and A. Derkachova, Impact of the interband transitions in gold and silver on the dynamics of propagating and localized surface plasmons, Nanomaterials **10**, 1411 (2020).

[41] K.-H. Lee and K. J. Chang, First-principles study of the optical properties and the dielectric response of Al, Phys. Rev. B **49**, 2362 (1994).

[42] W. Kohn, Wannier functions and self-consistent metal calculations, Phys. Rev. B **10**, 382 (1974).

[43] B. Sporkmann and H. Bross, Calculation of wannier functions for fcc transition metals by fourier transformation of bloch functions, Phys. Rev. B **49**, 10869 (1994).

[44] G. Prandini, M. Galante, N. Marzari, and P. Umari, Simple code: Optical properties with optimal basis functions, Comput. Phys. Commun. **240**, 106 (2019).

[45] G. Prandini, G.-M. Rignanese, and N. Marzari, Photorealistic modelling of metals from first principles, npj Comput. Mater. **5**, 129 (2019).

[46] M. Methfessel and A. T. Paxton, High-precision sampling for brillouin-zone integration in metals, Phys. Rev. B **40**, 3616 (1989).

[47] P. E. Blöchl, O. Jepsen, and O. K. Andersen, Improved tetrahedron method for brillouin-zone integrations, Phys. Rev. B **49**, 16223 (1994).

[48] C. Friedrich, S. Blügel, and D. Nabok, Quasiparticle self-consistent GW study of simple metals, Nanomaterials **12**, 3660 (2022).

[49] M. Cazzaniga, N. Manini, L. G. Molinari, and G. Onida, *Ab initio* self-energy corrections in systems with metallic screening, Phys. Rev. B **77**, 035117 (2008).

[50] M. Cazzaniga, L. Caramella, N. Manini, and G. Onida, *Ab initio* intraband contributions to the optical properties of metals, Phys. Rev. B **82**, 035104 (2010).

[51] O. K. Orhan and D. D. O'Regan, Plasmonic performance of $Au_xAg_yCu_{1-x-y}$ alloys from many-body perturbation theory, J. Phys.: Condens. Matter **31**, 315901 (2019).

[52] M. Khazaei, A. Ranjbar, M. Ghorbani-Asl, M. Arai, T. Sasaki, Y. Liang, and S. Yunoki, Nearly free electron states in MXenes, Phys. Rev. B **93**, 205125 (2016).

[53] V. Kamysbayev, A. S. Filatov, H. Hu, X. Rui, F. Lagunas, D. Wang, R. F. Klie, and D. V. Talapin, Covalent surface modifications and superconductivity of two-dimensional metal carbide MXenes, Science **369**, 979 (2020).

[54] K. Wang, H. Jin, H. Li, Z. Mao, L. Tang, D. Huang, J.-H. Liao, and J. Zhang, Role of surface functional groups to superconductivity in Nb_2C-MXene: Experiments and density functional theory calculations, Surf. Interfaces **29**, 101711 (2022).

[55] G. Guan and F. Guo, A review of Nb_2CT_x MXene: Synthesis, properties and applications, Batteries **9**, 235 (2023).

[56] A. Marini, C. Hogan, M. Grüning, and D. Varsano, YAMBO: An *ab initio* tool for excited state calculations, Comput. Phys. Commun. **180**, 1392 (2009).

[57] D. Sangalli, A. Ferretti, H. Miranda, C. Attaccalite, I. Marri, E. Cannuccia, P. Melo, M. Marsili, F. Paleari, and A. Marrazzo, Many-body perturbation theory calculations using the YAMBO code, J. Phys.: Condens. Matter **31**, 325902 (2019).

[58] P. Giannozzi, S. Baroni, N. Bonini, M. Calandra, R. Car, C. Cavazzoni, D. Ceresoli, G. L. Chiarotti, M. Cococcioni, and I. Dabo, QUANTUM ESPRESSO: A modular and open-source software project for quantum simulations of materials, J. Phys.: Condens. Matter **21**, 395502 (2009).

[59] P. Giannozzi Jr, O. Andreussi, T. Brumme, O. Bunau, M. B. Nardelli, M. Calandra, R. Car, C. Cavazzoni, D. Ceresoli, and M. Cococcioni, Advanced capabilities for materials modelling with quantum ESPRESSO, J. Phys.: Condens. Matter **29**, 465901 (2017).

[60] J. P. Perdew, K. Burke, and M. Ernzerhof, Generalized gradient approximation made simple, Phys. Rev. Lett. **77**, 3865 (1996).

[61] M. van Setten, M. Giantomassi, E. Bousquet, M. Verstraete, D. Hamann, X. Gonze, and G.-M. Rignanese, The pseudodojo: Training and grading a 85 element optimized norm-conserving pseudopotential table, Comput. Phys. Commun. **226**, 39 (2018).

[62] S. Grimme, Semiempirical GGA-type density functional constructed with a long-range dispersion correction, J. Comput. Chem. **27**, 1787 (2006).

[63] V. Hernandez, J. E. Roman, and V. Vidal, SLEPc: A scalable and flexible toolkit for the solution of eigenvalue problems, ACM Trans. Math. Softw. **31**, 351 (2005).

[64] See Supplemental Material at http://link.aps.org/supplemental/10.1103/PhysRevMaterials.8.075201 for S1. The optimised crystal structures of the systems under study; S2. The method used for the determination of the Drude model parameters; S3. The calculated real part of the dielectric function; S4. The calculated band structures and density of states of $Ti_3C_2T_2$ MXenes; S5. The dielectric function computed for the $Ti_3C_2T_2$ MXenes.

[65] S. Saha, T. P. Sinha, and A. Mookerjee, Electronic structure, chemical bonding, and optical properties of paraelectric $BaTiO_3$, Phys. Rev. B **62**, 8828 (2000).

[66] H. Zhang, D. Wu, Q. Tang, L. Liu, and Z. Zhou, Zno–gan heterostructured nanosheets for solar energy harvesting: Computational studies based on hybrid density functional theory, J. Mater. Chem. A **1**, 2231 (2013).

[67] D. Wang, C. Zhou, A. S. Filatov, W. Cho, F. Lagunas, M. Wang, S. Vaikuntanathan, C. Liu, R. F. Klie, and D. V. Talapin, Direct synthesis and chemical vapor deposition of 2D carbide and nitride MXenes, Science **379**, 1242 (2023).

[68] C. Sevik, J. Bekaert, and M. V. Milošević, Superconductivity in functionalized niobium-carbide MXenes, Nanoscale **15**, 8792 (2023).

[69] X. Zhang, L. Zhang, J. D. Perkins, and A. Zunger, Intrinsic transparent conductors without doping, Phys. Rev. Lett. **115**, 176602 (2015).

[70] S. K. Azadi, M. Zeynali, S. Asgharizadeh, and M. A. Fooladloo, Investigation of the optical and electronic properties of functionalized Ti_3C_2 MXene with halide atoms using DFT calculation, Mater. Today Commun. **35**, 106136 (2023).

[71] C. W. Chu, F. Chen, J. Shulman, S. Tsui, Y. Y. Xue, W. Wen, and P. Sheng, A negative dielectric constant in nano-particle materials under an electric field at very low frequencies, Strongly Correl. Electron Mater. Phys. and Nanoeng. **5932**, 59320X (2005).

[72] K. P. Singh and S. Bhattacharjee, Optical parameters of atomically heterogeneous systems created by plasma based low energy ion beams: Wavelength dependence and effective medium model, Front. Phys. **9**, 671137 (2021).

[73] M. M. Mridha and S. H. Naqib, Pressure dependent elastic, electronic, superconducting, and optical properties of ternary barium phosphides (BaM_2P_2; $M =$ Ni, Rh) : DFT based insights, Phys. Scr. **95**, 105809 (2020).

[74] K. Chaudhuri, M. Alhabeb, Z. Wang, V. M. Shalaev, Y. Gogotsi, and A. Boltasseva, Highly broadband absorber using plasmonic titanium carbide (MXene), ACS Photon. **5**, 1115 (2018).

[75] Y. Zuo, Y. Gao, S. Qin, Z. Wang, D. Zhou, Z. Li, Y. Yu, M. Shao, and X. Zhang, Broadband multi-wavelength optical sensing based on photothermal effect of 2D MXene films, Nanophotonics **9**, 123 (2020).

[76] Y. Chen, Y. Ge, W. Huang, Z. Li, L. Wu, H. Zhang, and X. Li, Refractive index sensors based on $Ti_3C_2T_x$ MXene fibers, ACS Appl. Nano Mater. **3**, 303 (2020).

[77] S. Adomavičiūtė-Grabusovė, S. Ramanavičius, A. Popov, V. Šablinskas, O. Gogotsi, and A. Ramanavičius, Selective enhancement of SERS spectral bands of salicylic acid adsorbate on 2D $Ti_3C_2T_x$-based MXene film, Chemosensors **9**, 223 (2021).